
Article:
Yao, J, Zhao, Y and Fairweather, M (2015) Numerical Simulation of Turbulent Flow Through a Straight Square Duct. Applied Thermal Engineering, 91. pp. 800-811. ISSN 1359-4311

https://doi.org/10.1016/j.applthermaleng.2015.08.065

Numerical simulation of turbulent flow through a straight square duct

Jun Yao[1,2], Yan Lin Zhao[1*], M. Fairweather[3]

[1]Beijing Key Laboratory of Process Fluid Filtration and Separation, College of Mechanical and Transportation Engineering, China University of Petroleum-Beijing, Beijing 102249, People's Republic of China

[2] College of Energy, Xiamen University, Xiamen 361005, People's Republic of China

[3]Institute of Particle Science and Engineering, School of Process, Environmental and Materials Engineering, University of Leeds, Leeds LS2 9JT, UK

* Corresponding Author:

Dr. Y. L. Zhao, College of Mechanical and Transportation Engineering, China University of Petroleum-Beijing, Beijing 102249, People's Republic of China

Telephone: +86 (0) 10 89733658; Facsimile: +86 (0) 10 89733658; Email address: ylzhao@cup.edu.cn

Abstract

Turbulent duct flows are investigated using large eddy simulation at bulk Reynolds numbers, from 4410 to 250000. Mean secondary flow are found to reveal the existence of two steamwise counterrotating vortices in each corner of the duct. Turbulence-driven secondary motions that arise in duct flows act to transfer fluid momentum from the centre of the duct to its corners, thereby causing a bulging of the streamwise velocity contours towards the corners. As Reynolds number increases, the ratio of centerline streamwise velocity to the bulk velocity decreases and all turbulent components increase. In addition, the core of the secondary vortex in the lower corner-bisector tends to approach the wall and the corner with increasing Reynolds number. The turbulence intensity profiles for the low Reynolds number flows are quite different from those for the high Reynolds number flows.Typical turbulence structures in duct flows are found to be responsible for the interactions between ejections from wall and this interaction results in the bending of the ejection stems, which indicates that the existence of streaky wall structures is much like in a channel flow.

Keywords: Duct flow; Secondary flow; Reynolds number; Turbulence; Large Eddy Simulation

1 Introduction

A greater understanding the mechanisms of liquid or solid-phases behave within fluid flows, and of their either impact on walls or dispersion and depositon, is important in many industrial environmental, and energy-related processes. Examples include the erosion of pipes [1,2], the cleaning of electronic chips, the handling of powders, the transmission of diseases and the transport of pesticides. Knowledge of liquid or solid-phases turbulent behaviour in ducts is more specifically of relevance both environmentally and industrially to flows in, for example, ventilations systems, heat exchangers and gas turbine cooling systems, and the ability to predict such behaviour is of value in more effective system design and operation. Of particular interest is the processing and transportation of nuclear waste, which is stored as a liquid-solid sludge, and its behaviour in terms of the steeling or nonsettling characteristics of particles, their propensity to form solid beds, and the deposition characteristics of particles in a bed. The formation of particle beds can result in blockages to pipes and equipment and lead to difficulties in obtaining dispersed particle flows from storage equipment for subsequent processing. The pumping of waste along pipes or ducts also gives rise to highly complex flows, where secondary flows caused , for example, by pipe bends can induce particle deposition. An understanding of how these flows behave during transportation is of clear benefit to more cost-effective process design, continued operation, and accelerated waste clean-up. The safer and more efficient processing of liquid or solid-phase, in particular, provides the motivation for the current work.

Many industrial applications of duct could be found in heat exchanger, chemical reactor, burner and so on. Jin et al. [1] first applied direct numerical simulation (DNS) method to study tubes located in the middle of duct with row of a 10x10 aligned tube bank together with considering coal ash particles collision and erosion. Yao et al.[2] applied experimental method to investigate the erosion of stainless steel by two-phase impinging jet and indicated that the flow turbulence plays an important role in causing the amount of erosion. Cheng et al. [3] used numerical simulations to investigate the flow in

three-dimensional straight square micro-channels containing superhydrophobic surfaces patterned with square posts, square holes, transverse, or longitudinal grooves. The effects of pattern width to channel height ratio and the Reynolds number on the effective slip length are analyzed in detail for different shear-free fractions. Furthermore, Cheng et al. [4] investigated the frictional and thermal performance for the same structure as a promising candidate for electric cooling. Al-Bakhit and Fakheri [5] studied a parallel flow heat exchanger in rectangular ducts to determine the impact of different parameters on the performance and the accuracy of constant heat transfer coefficient assumption. They found that the performance of the heat exchanger primarily depends on the flow in the ducts, i.e. the fluid properties and the mass flow rate and aspect ratios. The importance of the duct flow necessitates the examination of the impact of developing velocity profiles on the heat exchanger performance.

It is clear that the turbulent flow inside a duct of square or rectangular cross-section is of considerable engineering interest. This flow is characterized by the existence of secondary flows (Prandtl's flow of the second kind) which are driven by the turbulent motion. The problem of secondary flows developing under transitional and turbulent conditions in ducts of triangular or rectangular cross section has also attracted much attention due to the significance in engineering practice.The secondary flow is a mean flow perpendicular to the main flow dirction. It is relatively weak (1-3% of the mean streamwise velocity), but its effect on the transport of momentum is quite significant.

A number of numerical simulations of the turbulent flow in a square duct have been reported over the last three decades. Many earlier efforts used the Reynolds-avearged Navier-Stokes (RANS) equations in conjunction with a closure model for the Reynolds stresses. As expected, those closure models based on assumptions of isotropy, such as the conventional k-ε and k-ω models failed to predict any turbulence-driven secondary flow. The earliest successful attempt was probably obtained by Launder and Ying [6]. In their study, the algebraic Reynolds stress model was used to solve for the cross-stream flow. Similar studies followed subsequently. The difference in these studies is the forms

for modeling the various terms in the differential Reynolds stress transport equations, notably the pressure-strain correlations. Nisizima and Yoshizawa [7] used non-linear forms of the k-ε equations to account for the aniso-tropy in the Reynolds normal stresses and were able to predict the existence of secondary flows in square ducts. All these numerical simulations have been able to capture the existence of secondary flows in general but the comparison of turbulence quantities with experimental data was not completely satisfactory. The disagreement is probably due to the empiricism involved in modeling the various correlations in the transport equations. In recent years, with the development of computer technology as well as high capability computation methods, it is possible to investigate single duct flows in smaller turbulent scales using high-quality modeling methods, for example, direct numerical simulation and large eddy simulation. Gavrilakis [8] performed a direct numerical simulation (DNS)at a Reynolds number (based on bulk values)of Re_b=4410. A second-order finite volume scheme and a fractional step method were used with up to 1.6×10^7 grid points. Gavrilakis' simulations were in reasonable agreement with the mean flow and turbulence statistics obtained from experiments of Niederschulte et al. [9]. Such DNS does not need any turbulence structures. Since DNS resolves all the length scales, the computational demands are very large and therefore limited to low Reynolds numbers. As a compromise between RANS and DNS, large eddy simulation (LES) was used to study the flows in a square duct by Madabhushi and Vanka[10]. Comparison between the LES and DNS results clearly demonstrate that LES is capable of capturing most of the energy carried by turbulence eddies and can accurately predict the generally accepted pattern of the turbulence-driven secondary flow. Although some issues still need to be resolved, such as subgrid-scale (SGS) modeling and grid resolution for high Reynolds number flows, the results can be quite accurate if the subgrid scales do not contain much energy. Thus, LES has the advantage of reducing empiricism ove the Reynolds-averaged approach and reducing computional burden over the DNS.

Since the appearance of secondary mean motion of a turbulent flow in a straight duct flow was first measured indirectly by Nikuradse [11], a large number of experimental studies have been conducted to elucidate the dynamic response of the mean flow to the highly anisotropic turbulent field in the vicinity of an internal corner [12]. The importance of the turbulence anisotropy and the turbulent shear stress component associated with the secondary mean flow field was early recognized. However, the experimental uncertainty related to measuring the important secondary shear stress component prevents firm conclusions to be drawn. Certain issues are not fully addressed owing to limitations of experimental investigations, for example, the resolution of the flow very near the free surface. The origin of the inner secondary flow in the context of vorticity transport, the role played by the diverging surface current found when studying jets, wakes or boundary layers parallel to a free surface [13], the vortex structures in a turbulent mixed-boundary corner, are examples of the questions, which are not yet conclusively investigated. Many of the discrepancies are probably due to the different set-ups in the different studies, as also mentioned by Grega et al. [14]. High-resolution DPIV measurements [14] made in the cross-stream plane used the same experimental apparatus as two earlier works by the authors. It was found that there was an, as yet, undetermined source of streamwise vorticity particularly in the outer secondary flow region closed to the free surface.

All above studies have demonstrated that turbulence-driven secondary motions, which arise in duct flows, act to transfer fluid momentum from the centre of the duct to its corners, thereby cause a bulging of the streamwise velocity contours towards the corners. They also established that the Reynolds normal and shear stresses contribute equally to the production of mean streamwise vorticity. In such flows, therefore, the directions normal to the streamwise direction are inhomogeneous and wall-bounded, unlike for the widely studied plane channel flow.

The paper is organized as following. In the next section, the mathematical model and subgrid-scale model used are briefly described. Then, the results of a closed-duct

calculation is presented to validate the code. Discussion of the mean flow field includes mean velocities, streamwise flow, secondary flow and the turbulent flow field, which includes turbulent intensities and instantaneous flow. Finally, conclusions are drawn in the last section.

2. MATHEMATICAL MODEL

2.1. Flow configuration

A schematic diagram of the duct geometry and co-ordinate system used is given in Fig. 1. The flow considered is three-dimensional and described using a Cartesian co-ordinate system (x, y, z) in which the z axis is aligned with the streamwise direction, the x axis is in the direction normal to the floor of the duct, and the y axis is in the spanwise direction. The corresponding velocity components in the (x, y, z) directions are (u, v, w), respectively. In modelling this flow, the boundary conditions for the momentum equations were no-slip at the duct walls. The specification of inflow and outflow conditions at the open boundaries of the duct was avoided by assuming that the instantaneous flow field was periodic along the streamwise direction, with the pressure gradient that drove the flow adjusted dynamically to maintain a constant mass flux through the duct.

The Navier-Stokes equations were solved numerically in a square cross-sectioned domain of size $2h \times 2h \times 8\pi h$ in the x, y and z directions, respectively. The length of the duct was sufficiently long to accommodate the streamwise-enlongated, near-wall structures present in wall-bounded shear flows, with such structures rarely expected to be longer than approximately 1,000 wall units [15].

The physical domain was discretized using between 4.50×10^5 and 1.44×10^6 grid points in all the Reynolds number flows examined. Compared with the 2.0×10^6 nodes used by Huser and Biringen [16] in their DNS of the low lowest Reynolds number flow considered, present LES are therefore relatively highly resolved on the basis of the maximum number of nodes noted above, and approximately 75% of that number. All discretizations were

uniform in the streamwise (z) direction, whereas in the vertical and spanwise directions (x and y, respectively) grid points were clustered towards the walls. In particular, for all simulations, the point closest to the wall was placed at x^+ or y^+=0.37-6.39, with on average 5 nodes in the near-wall region (x^+ or y^+<10). Other simulations using an increased total number, and alternative distributions, of non-uniformly distributed nodes were also used to give better resolution near the walls of the duct, further details of which could be found in Fairweather and Yao [17] and Yao and Fairweather [18]. These sensitivity studies did, however, demonstrate that the discretizations noted above resulted in turbulence statistics, in those regions of the duct of interest herein, that were independent of grid resolution. The flows investigated had bulk Reynolds numbers, $Re_b=w_b h/\nu$, of 4410 to 250,000, defined using the cross-stream, area-averaged streamwise velocity, with equivalent friction Reynolds numbers, $Re_\tau=u_\tau h/\nu$, of 300 to 10550, respectively.

2.2. Large Eddy Simulation

In LES only the large-scale parts of the velocity and scalar fields are computed and the effects of the subgrid scales are modelled. To achieve this，a spatial filter was applied to the equation of motion: the spatial filter of a function $f=f(\mathbf{X}, t)$ was defined as it convolution with a filter function, G, according to

$$\overline{f}(X,t)=\int_{\Omega} G(X-X';\lambda(X))f(X',t)dX' \qquad (1)$$

where the filter function must be positively definited to maintain filtered values of scalars such as the mass fraction within bound values and the integration was defined over the entire flow domain Ω. The filter function had a characteristic width of λ, which, in general, might vary with the position.

Applying Eq. (1) to the Navier-Stokes equations for an incompressible Newtonian fluid with constant properties, under the hypotheses that filtering and differentiation in space commute, gave:

Continuity:

$$\frac{\partial \overline{u}_j}{\partial x_j} = 0\,, \tag{2}$$

Momentum:

$$\frac{\partial \overline{u}_i}{\partial t} + \frac{\partial \overline{u}_i \overline{u}_j}{\partial x_j} = -\frac{1}{\rho}\frac{\partial \overline{p}}{\partial x_i} + \frac{\partial}{\partial x_j}\left[\nu\left(\frac{\partial \overline{u}_i}{\partial x_j} + \frac{\partial \overline{u}_j}{\partial x_i}\right)\right] - \frac{\partial \tau_{ij}}{\partial x_j} \tag{3}$$

In Eq. (3), ρ is the constant fluid density, u_i is the velocity component in the x_i direction, p is the pressure and v is the assumed constant kinematic viscosity and $\tau_{ij} = \overline{u_i u_j} - \overline{u}_i \overline{u}_j$ represents the effect of the sub-grid scale motions on the resolved scale motions. This term, known as the sub-grid scale stress, must be modelled in order to solve the filtered equations.

The dynamic sub-grid scale stress model [19] was used in this work, implemented using the approximate localization procedure [20] together with the modification proposed by di Mare and Jones [21]. This represents the sub-grid scale stresses as the product of a sub-grid scale viscosity, v_{sgs}, and the resolved part of the strain tensor, with v_{sgs} evaluated as the product of the filter length Δ times an appropriate velocity scale, taken to be $\Delta\|\overline{s}\|$. The anisotropic part of the sub-grid scale stresses is given by: $\tau_{ij}^a = -2\left(C\Delta\right)^2 \|\overline{\mathbf{s}}\| \overline{s}_{ij}^a$,where the model parameter C must be determined. In the dynamic model this is achieved by applying a second filtering operation, denoted by, to Eq. (3). In the test filtered equation the sub-grid scale stresses are: $T_{ij} = \widehat{\overline{u}_i u_j} - \tilde{\overline{u}}_i \tilde{\overline{u}}_j$, and hence : $L_{ij} = T_{ij} - \tilde{\tau}_{ij} = \widehat{\overline{u}_i}\overline{u}_j - \tilde{\overline{u}}_i \tilde{\overline{u}}_j$. This expression is known as Germano's identity, and involves only resolved quantities. To evaluate C, some forms of relationship between the model constant values C and $C^2(\tilde{})$ at the grid- and test-filter levels must be specified. Based on the hypothesis that the cut-off length falls inside the inertial sub-range, the expression generally used is: $C^2 = C^2\left(\tilde{}\right)$.

Such a sub-range is not, however, guaranteed to occur in wall-bounded or low Reynolds number flows, with the largest deviations from universality of the sub-grid scale motions occurring in the regions of weakest resolved strain. Values of the model parameter at different filter levels are therefore likely to differ, and to account for this di Mare and Jones [21] proposed that:

$$C^2\left(\tilde{}\right) = C^2\left(1 + \frac{\varepsilon}{2\sqrt{2}\Delta^{\tilde{}2}\left\|\tilde{\bar{s}}\right\|\left\|\tilde{\bar{s}}^a\right\|^2}\right). \tag{4}$$

In Eq.(4), ε has the dimensions of dissipation and, assuming the flow to have only one length scale l and velocity scale v: $\varepsilon \approx v^3/l$, with v taken as the bulk velocity and l the half-width of the square duct.

Eq. (4) assumes that the scale invariance of *C* can only be invoked if the cut-off falls inside an inertial sub-range, and when this occurs the modelled dissipation should represent the entire dissipation in the flow. Conversely, in the high Reynolds number limit, the dissipation is only determined by v and l, so that the ratio of ε to $\Delta^{\tilde{}2}\left\|\tilde{\bar{s}}\right\|^3$ measures how far the flow is from scale preserving conditions. This equation is a first-order expansion of other scale-dependent expressions for *C*, e.g. Porte-Agel et al.[22], which also use a single length and velocity scale. $L_{ij} = T_{ij} - \tilde{\tau}_{ij} = \widetilde{\bar{u}_i}\bar{u}_j - \tilde{\bar{u}}_i\tilde{\bar{u}}_j$ and Eq. (4), with contraction of both sides with the tensor $\tilde{\bar{s}}$, then give:

$$C^2 = \frac{\left[2\sqrt{2}\left(C_*^2\Delta\right)^2\left\|\bar{\mathbf{s}}\right\|\left\|\bar{s}_{ij}^a\right\|^{\tilde{}}\,\tilde{\bar{s}}_{ij}^a - L_{ij}^a\tilde{\bar{s}}_{ij}^a\right]}{\varepsilon + 2\sqrt{2}\Delta^{\tilde{}2}\left\|\tilde{\bar{s}}\right\|\left\|\tilde{\bar{s}}^a\right\|^2}, \tag{5}$$

where C_*^2 is a provisional value for C^2, i.e. its value at the previous time step [20]. Eq. (4) gives a simple expression for C^2 whose evaluation requires only minor modifications to the approximate localization procedure. The advantage of the method is that it is well conditioned and avoids the spiky and irregular behaviour exhibited by some implementations of the dynamic model. In addition, as the resolved strain tends to zero,

C^2 also tends to zero, whilst $C^2(\tilde{})$ remains bounded. Eq. (5) also yields smooth C^2 fields without averaging, and the maxima of C^2 are of the same order of magnitude as Lilly's [23] estimate for the Smagorinsky model constant. The approach does not, however, prevent negative values of the model parameter, with such values being set to zero to prevent instability. Negative values of the sub-grid scale viscosity are similarly set to zero. Test-filtering was performed in all space directions, without averaging of the computed model parameter field. The ratio $\tilde{\Delta}/\Delta$ was set to 2, and the filter width was determined from $\Delta = \left(\Delta_x \Delta_y \Delta_z\right)^{1/3}$.

Computations were performed using the computer program BOFFIN. The code implemented an implicit finite-volume incompressible flow solver using a collocated variable storage arrangement. Because of this arrangement, fourth-order pressure smoothing, based on the method [15], was applied to prevent oscillations in the pressure field. Time advancement was performed via an implicit Gear method for all transport terms, and the overall procedure is second-order accurate in space and time. A constant time step was chosen, requiring the maximum Courant number to be lied between 0.1 and 0.3, with this enforced for reasons of accuracy. Time-averaged flow field variables reported later were computed from running averages during the computations.

2.3 Boundary conditions

2.3.1 Inflow conditions

The specification of inflow conditions is straightforward for transitional flows: only the mean flow and a desired perturbation must be prescribed. The same technique can be used for fully developed flows, but the length required for the perturbation to develop completely and the flow to reach the final state can be considerable. A fluctuating signal can be generated by adding rotating and oscillating helical perturbations to an assigned mean flow:

$$u(x,t) = U_m + \sum_{i=1,N} A_i \sin(\alpha_i + |k|_i x) + \sum_{i=1,N} B_i \cos(\alpha_i + |k|_i x) \qquad (6)$$

where the phase α and frequency $|k|_i x$ of each mode are chosen randomly, the latter on a spherical shell of radius $|k|$ in wave number space. The coefficients A_i and B_i can be determined by enforcing continuity.

2.3.2 Outflow Conditions

The ideal requirement for the outflow boundary is that disturbances originated at the domain outlet be converted out of it without being propagated upstream. A common practice is to assign a zero gradient condition (also referred to as reflective) on the boundary:

$$\left.\frac{\partial u_j}{\partial n}\right|_{\Gamma}=0 \qquad (7)$$

where *n* is the outward normal to the boundary surface. For the convective fluxes this corresponds to a first order upwind approximation. This is generally sufficient to minimise the effects of the boundary on the solution if the flow can be considered approximately parabolic in the outlet region.

3 Results analysis

3.1 The mean flow field

3.1.1 Mean velocities

We have verified our numerical procedure through comparisions with the experimental data on a similar geometry presented by Cheesewright et al [24]. These comparisons are presented in Figs 2, 3, where the *y/h* label represents the distance from the wall. In Figs 2,3, the solid lines represent the present LES data and the circles represent the experimental measurement.

The flow statistics were obtained over a long computation time. Geometrical (and flow) symmetry and homogeneity along the *z*-direction were exploited while computing the quadrant-averaged data. Fig.2 (a) displays the quadrant-averaged profiles of the mean streamwise velocity components at five locations of the square duct. All of the velocity

profiles in Fig.2(a) are normalized by the mean value of the streamwise velocity at the duct centerline, w_0. A short experimental study of the turbulent flow through a square duct was carried out by Cheesewright, McGrath & Petty [24]. Their Reynolds number based on the centerline velocity and duct side is $Re_0=2hU_0/v$= 4900 which is close to that of the simulation, 4410. The agreement between measurements and simulation for points in the flow at distances greater than 0.1h from the nearest wall is excellent. Outside these limits the measured U-values are quite asymmetric with respect to the corner bisector with velocities differing by as much as 20%. Fig.2(b) displays the mean spanwise velocity components at five locations, which clearly indicates the presence of the secondary flows. Their location and magnitude are very well reproduced by our LES. Note that the mean secondary flow is relatively weak (1-2% of the bulk streamwsie velocity). Because the simulation results are symmetric to within 4% it is inferred by comparing the zero crossing of the two sets of data-that the secondary flow cells of the experiment are also asymmetric about the corner bisector. Due to the smaller magnitude of spanwise velocity, the agreement of simulation and experimental seems not as well as that of streamwise velocity.

3.1.2 Streamwise flow

Fig.3 (a) shows a comparison between the present predictions and axial mean velocity profiles measured along wall of a square duct at five downstream stations. The predictions are compared mainly with the data of Gessner et al.[25] and Gessner and Emery[26]. Note that the difference between them is a good measure of the experimental scatter, since they were obtained in the same expeiemental apparatus and undere similar conditions. It can be seen that the predicted distributions along the wall are in good agreement with their experimental counterparts as a whole, particularly when the data [26] are taken for comparison.

The streamwise development of axial mean velocity in a square duct at Re_b=250,000 is shown in Fig.3(b). The distributions apply at eight distances from the wall over the

interval 0.01≤*x*/h≤0.5 along the wall bisector (*y*/h=0.5) of the duct. In reference to Fig.3(b), it can be seen that present LES performs reasonably well for predicting local flow development along the wall bisector. The figure indicates that the velocities in the central region increase first with streamwise distance, reach local peak values, and then decrease to asymptotic values. The local peak in the central region is not a secondary flow effect, but the result of shear layer interactions which occur as the boundary layers on opposite walls of the duct merge. On the contrary, the velocities near the wall directly decrease to their asymptotic values without increasing, due to the presence of the wall. In particular, the peak of the centerline velocity occurs downstream of the location where the boundary layers begin to merge (*z*/h=32), indicating that further adjustment of the flow takes place after the core flow becomes nonexistent. This is presumably due to the shear layer interaction effects which lead to a non-equilbrium condition at about *z*/h=32 [26].

The effect of Reynolds number on steamwise velocity is shown in Fig.4 where the velocities normalized with bulk velocity along the lower wall bisector (*y*/*h*=1) are plotted. It can be seen that the ratio of centerline streamwise velocity to the bulk velocity decreases with increasing Reynolds number. This is because the profiles of streamwise velocity become flatter and the gradients in the wall region become steeper due to increased turbulent mixing at higher Reynolds numbers. The calculated profile is consistent with this trend. Fig.4 also demonstrates the fact that the present LES results are in reasonable agreement with those of duct flow studies [8,25].

3.1.3 Secondary flow

In addition to the mean velocity and streamwsie velocity, the secondary flow is an important quantity by which the quality of the simulation can be assessed. The contours of mean (averaged) streamwise volicity are shown in Fig.5 (a) for Re_b =35500. In order to obtain the best statistical averages, the secondary velocity vectors, averaged over the four quadrants are shown in Fig.5 (b). In Fig.5(a), the mean streamwise velocity is

directed away from us. The mean secondary flow vectors (shown in Fig.5(b)) reveal the existence of two steamwise counterrotating vortices in each corner of the duct. The distribution of the streamwise velocity contours in the vicinity of the corner is due to the momentum transfer by the secondary flows from the core of the duct toward the corner. The predominant effect of the secondary motion is the induced transport of streamwise momentum towards the corner region; the isolevels of the mean streamwise velocity nearest the wall become slightly distorted (see Fig.5(a)). The isotachs are bent toward the corner, indicating a magnitude increase for the mean streamwise velocity. A high degree of symmetry about the corner bisector can be seen in this Figure. The maximum secondary velocity in the current simulation is about 2.4% of the bulk velocity while Brundrett and Baines reported a value of 2.2%.

In present work, the locations of the secondary vortex are found on ($2x/h$, $2y/h$)=(0.20, 0.51) and (0.17,0.44) for Re_τ=300 and 600, respectively. They are in good agreement with the locations (0.22, 0.52), (0.24, 0.56)and (0.17, 0.44) observed in DNS at Re_τ=300 [8], LES at Re_τ=360 [10], and DNS at Re_τ=600 [16], respectively. Note that the Reynolds numbers based on the wall-averaged friction velocities are 300, 360 and 600 in the previous duct flow Gavrilakis [8], Madabhushi and Vanka [10] and Huser and Biringen [16], repectively. The mid-wall friction velocity based scaling is more appropriate for comparing the turbulence statistics along the wall-bisector.

The secondary flow velocity vectors and streamwise mean velocity contours given in one quadrant of the square duct for three Reynolds numbers (Re_b= 10320, 83000 and 250000) are ploted in Fig.6. Regardless of Reynolds number effect, the secondary flows first impinge on the corners along the bisectors and then accelerate along the walls for some distance before turning away from the walls. At the wall bisector, the present results exhibit a local maximum for the mean streamwise velocity whereas a local minimum exists in high-Reynolds-number experiments [12] (Talbe 1) that list the Reynolds numbers of the computational and experimental studies for duct flows. The occurance of a local streamwise velocity maximum at the wall bisector is a low-

Reynolds-number effect [8]. It is clear that the secondary flow consists of a streamwise counter-rotating vortex pair around the corner of the square duct. The secondary flow distorts the isovels towards the corner and increases corner bisector momentum transfer. In comparison with the secondary flows in terms of various Reynolds number, as shown in Fig. 6 (a)-(c), it is found that as the Reynolds number increases, these secondary flows penetrate more into the corner region and the region of acceleration along the wall is closer to the corner. In brief, the core of the secondary vortex in the lower corner-bisector tends to approach the wall and the corner.

3. 2 The turbulent flow field

3. 2.1 Turbulent intensities

A direct comparison of the intensities along the *x* direction at five different sections, i.e. *y/h*=0.1(0.16), 0.3, 0.5, 0.7, and 1.0(0.8), from simulation and square-duct experiments [24] is made in Fig.7, where the turbulence intensities are normalized by the mean streamwise velocity at the center of the duct (W_0).

It can be seen in Fig.7 that the turbulence intensities in the present LES agree well with the results by Cheesewright et al. [24] for all sections. In the middle plane (y/h=1.0), a strong turbulent activity is observed: the velocity intensities profiles exhibit trends which are very similar to standard turbulent channel flows or boundary layers. Indeed, the W_{rms} component dominates the V_{rms} component with a very marked peak close to the wall. In the vicinity of the wall, all velocity intensities values decrease with approaching the corner and a very low level of turbulent activity reaches. The profiles of W_{rms} at y/H=0.1 (Fig.7(b)) are different from those at other sections. That is, W_{rms} becomes a local minimum near the corner bisector after its peak, which is the effect of the secondary flows along the corner bisector. Since these secondary flows transport lumps of low turbulence from the center of the duct towards the corner, W_{rms} becomes the local minimum along the corner bisector. For V_{rms} (Fig.7(a)), the profile of V_{rms} at y/H=0.16 is slightly different from those at other sections. It is seen that along *y* direction with *y/h*

increasing (apart from the side wall), a peak value will appear near the duct bottom (low *x/h*) and the location of peak increases with *y/h*, which is due to the secondary effect.

Fig.8 shows three components of turbulence intensity normalized by the local friction velocity at the wall bisector. The distributions of W_{rms} and V_{rms} are similar to those at the place far from the side wall (y/h>0.5) as seen in Fig.7. In Fig.8, DNS data [8] and experimental data [24] are provided for comparisons with the present LES data at Re_b=4410. It can be seen in Fig.8 that the turbulence intensities from the present LES data agree well with DNS data [8] and with measured data [24] except for the peak value. This discrepancy may be caused by the difficulty in the measurement close to the wall. The profiles of all components of turbulence intensity from the present LES data at Re_b=250,000 appear to be obviously lager than the profiles from the cases at Re_b =4410 either by simulations or by experiment. Therefore, it can be concluded that all components increase with Reynolds number. Antonia et al [27] indicated that, for the channel flow, the Reynolds number dependence for *z*-component turbulent intensity is significant compared to that for *x*-component turbulent intensity and *y*-component turbulent intensity. In the present results, for the duct flow, not only *z*-component turbulent intensity but also *x*- and *y*-component turbulent intensity is enhaced with increasing Reynolds number. Especially, the wall-normal and spanwise components are enhanced. This is because that increasing Reynolds number, the energy redistribution increases remarkably for *x*- and *y*-component turbulent intensity, the increased turbulent mixing in the transverse plane resulting in higher fluctuations in the instantaneous secondary velocities. The difference in the peak comes from the Reynolds number effect that all components of turbulence intensity increase with Reynolds number in the log region of wall-bounded turbulent flows [28]. The difference in the other part of the profile also results from the same effect. Moser et al. [29] observed Reynolds number dependencde of the turbulence intensity profiles in their DNS of plane channel flows. That is, Moser et al. [29]

found that the turbulence intensity profiles for flows at high Reynolds numbers are extremely similar, however, the turbulence intensity profile for the low Reynolds number flow, similar to the flow simulated in the present study, is quite different from those for high Reynolds number flows.

3.2.2 Instantaneous flow

3.2.2.1 Instantaneous velocities

An instantaneous flow field at the $z=z_0/2$ plane is plotted in Fig.9. This result illustrates that the instantaneous flow field can be significantly different from and stronger than the averaged field (shown in Fig.5). For the sake of clarity, not all points in the wall region are plotted in these Figures. Fig.9 presents an illustrative cross-section of the instantaneous turbulence structures which contribute to the production of shear stresses. It shows that an ejection, which is not influenced by the sidewalls, appears at x/h=0.5 near the horizontal wall. In addition, the characteristic mushroom-like shape is depicted in Fig.9 (b) (x/h=0.5) and two counter-rotating vortices exist at the same place in Fig.9(a). Near the lower left corner, several ejections can be observed. The strongest ejection, whose mushroom shape is evident in Fig.9(b), starts from the horizontal wall at around x/h=0.35. The velocity vectors display two counter-rotating vortices, one at left and one at right of this ejection structure. The right vortex is most pronounce, and it appears that this vortex interacts with another ejection structure from the horizontal wall. Fig.9 (b) indictates that an ejection event is starting at around x/h=1.5 from the horizontal wall, and the stem of this ejection stretches out toward left along the horizontal wall and joins the right vortex belonging to the stronger ejection from the horizontal wall.

It must be emphasized that these instantaneous figures only serve as an example of typical turbulence structures in this flow which are responsible for the interactions between ejections from wall; this interaction results in the bending of the ejection stems.

3.2.2.2 Instantaneous turbulent fluctuations

Fig.10 shows the contours of the resolved instantaneous fluctuating velocities ($\overline{u''}$, $\overline{v''}$, $\overline{w''}$) in the *y*-*z* plane at x^+=8 (*x*/*h*=0.4). The solid lines represent positive velocities (greater than the mean) and the dotted lines represent negative velocities (less than the mean). Positive $\overline{u''}$ and $\overline{v''}$ velocities represent fluid moving away from (toward) the *x*/*h*=0 (*x*/*h*=2) and *y*/*h*=0 (*y*/*h*=2) walls, respectively. Negative $\overline{u''}$ and $\overline{v''}$ velocities represent fluid moving away from (toward) the *x*/*h*=2 (*x*/*h*=0) and *y*/*h*=2 (*y*/*h*=0), respectively. The current results indicate the existence of streaky wall structures much like in a channel flow. These streaks represent the impingement of high momentum fluid on the wall (sweeps, represented by positive $\overline{w''}$ and negative $\overline{v''}$ at the lower wall) and the ejection of low momentum fluid from the wall (bursts, represented by negative $\overline{w''}$ and positive $\overline{v''}$).

4 Conclusions

In this work, turbulent duct flows are investigated using large eddy simulation in a large range of Reynolds numbers. Conculsions could be obtained as following.

1) Secondary flows were successfully captured in the ducts although they are relatively weak (1-2% of the bulk streamwise velocity). It is confirmed that turbulence-driven secondary motions that arise in duct flows act to transfer fluid momentum from the centre of the duct to its corners, thereby causing a bulging of the streamwise velocity contours towards the corners. They consist of a streamwise counter-rotating vortex pair around the corner of the square duct.
2) As the Reynolds number increases, secondary flows penetrate more into the corner region and the region of acceleration along the wall is closer to the corner. It can be seen that the ratio of centerline streamwise velocity to the bulk velocity decreases with increasing Reynolds number.

3) All components turbulent intensity increases with Reynolds number. Especially, the wall-normal and spanwise components enhance with it. It is found that the turbulence intensity profiles for the low Reynolds number flows are quite different from those for the high Reynolds number flows.
4) Typical turbulence structures in turbulent duct flows are found to be responsible for the interactions between ejections from wall; this interaction results in the bending of the ejection stems, which indicates that the existence of streaky wall structures is much like in a channel flow.

Acknowledgement

This work was supported by National Natural Science Foundation of China (No. 51376153; 51406235), Science Foundation of China University of Petroleum, Beijing (No. 2462013YJRC030). The authors would also like to express their gratitude to Prof W.P. Jones for providing the BOFFIN LES code and for many helpful discussions on its use.

Nomenclature

A_i coefficient, dimensionless

B_i coefficient, dimensionless

C model parameter, dimensionless

f *a* spatial filter function, dimensionless

G a filter function, dimensionless

h width of square duct, *m*

k coefficient, dimensionless

n outward normal to the boundry surface, dimensionless

p pressure, N/m^2

Re flow Reynolds number, dimensionless

Re_b Reynolds number based on flow bulk velocity, dimensionless

Re_τ	Reynolds number based on flow friction velocity, dimensionless
t	time, s
u, v, w	velocity components in (x, y, z) directions, $m\ s^{-1}$
$\overline{u''}$, $\overline{v''}$, $\overline{w''}$	instantaneous fluctuating velocity components in (x,y,z) directions, $m\ s^{-1}$
u_i	the velocity component in the x_i direction, $m\ s^{-1}$
U_m	the mean velocity component in the x direction, $m\ s^{-1}$
$U_{rms}, V_{rms}, W_{rms}$	turbulence intensities components in (x, y, z) directions, $m\ s^{-1}$
u_τ	shear velocity, $m\ s^{-1}$
V	fluid velocity (u,v,w), $m\ s^{-1}$
w_0	the mean streawise velocity at the center of the duct, $m\ s^{-1}$
w_b	bulk flow velocity in streamwise direction, $m\ s^{-1}$
x, y, z	Cartesian co-ordinate system, m
x^+, y^+, z^+	Cartesian co-ordinate system in wall units, dimensionless

Greek letters

α	phase coefficient, dimensionless
ρ	fluid density, $kg\ m^{-3}$
v	kinematic viscosity, $m^2\ s^{-1}$
τ_{ij}	sub-grid scale stress, dimensionless
ν_{sgs}	sub-grid scale viscosity, dimensionless
Ω.	entire flow domain, dimensionless
λ	a characteristic width of filter function, dimensionless

References

[1] T. Jin, K. Luo, F. Wu, J. S. Yang, J. R. Fan,Numerical investigation of erosion on a staggered tube bank by particle laden flows with immersed boundary method. Appl Therm Eng 62(2014) 444-454.

[2] J. Yao, F. Zhou, Y. L. Zhao, H. Yin, N. Li, Investigation of erosion of stainless steel by two-phase jet impingement. Appl Therm Eng(2014) http://dx.doi.org/10.1016/j.applthermaleng. 2014.08.056 .

[3] Y. P. Cheng, C. J. Teo, B. C. Khoo, Microchannel flows with superhydrophobic surfaces: effects of Reynolds number and pattern width to channel height ratio Phys Fluid 21 (2009) 122004

[4] Y. P. Cheng, J. L. Xu, Y. Sui, Numerical study on drag reduction and heat transfer enhancement in microchannels with superhydrophhobic surfaces for electronic cooling Appl Therm Eng (2014) http://dx.doi.org/10.1016/j.applthermaleng. 2014.10.058

[5] H. Al-Bakhit, A. Fakheri, Numerical simulation of heat transfer in simultaneously developing flows in parallel rectangular ducts. Appl Therm Eng 26 (2006) 596-603.

[6] B. E. Launder, W. M. Ying, Secondary flows in ducts of square cross-section. J. Fluid Mech. 54 (1972) 289-295.

[7] S. Nisizima, A. Yoshizawa, Turbulent channel and Couette flows using an anisotropic k e. AIAA J 25 (1987) 414-420.

[8] S. Gavrilakis, Numerical simulation of low-Reynolds-number turbulent flow through a straight square duct. J. Fluid Mech. (1992) 244, 101-129.

[9] M. A. Niederschulte, R. J. Adrian, T. J. Hanratty, Measurements of turbulent-flow in a channel at low Reynolds-numbers. Exp. Fluids 9(1990) 222-230.

[10] R. K. Madabhushi, S. P. Vanka, Large eddy simulation of turbulence-driven secondary flow in a square duct. Phys. Fluids A. 3 (1991) 2734-2745.

[11] J. Nikuradse, Untersuchungen uber die Geschwindigkeitsverteilung in turbulenten Stromungen. PhD thesis, Göttingen, VDI Forsch. 281(1926).

[12] E. Brundrett, W. D. Baines, The production and diffusion of vorticity in duct flow. J. Fluid Mech. 19 (1964) 375-394.

[13] D. T. Walker, On the origin of the 'surface current' in turbulent free-surface flows. J. Fluid Mech. 339 (1997) 275-285.

[14] L. M. Grega, T. Y. Hsu, T. Wei, Vorticity transport in a corner formed by a solid wall and a free surface. J. Fluid Mech. 465 (2002) 331-352.

[15] C. M. Rhie, W. L. Chow, Numerical study of the turbulent-flow past an airfoil with trailing edge separation. AIAA J. 21(1983) 1525-1532.

[16] A. Huser, S. Biringen, Direct numerical-simulation of turbulent-flow in a square duct. J. Fluid Mech. 257(1993) 65-95.

[17] M. Fairweather, J. Yao, Mechanisms of particle dispersion in a turbulent, square duct flow. AIChE J. (2009) 55, 1667-1679.

[18] J. Yao, M. Fairweather, Inertial particle resuspension in a turbulent, square duct flow. Phys. Fluids 22(2010) 033303.

[19] M. Germano, U. Piomelli, P. Moin, W. Cabot, A dynamic subgrid-scale eddy viscosity model. Phys. Fluids A 3(1991) 1760-1765.

[20] U. Piomelli, J. Liu, LES of rotating channel flow using a localised dynamic model. Phys. Fluids 7 (1995) 839-848.

[21] F. Di Mare, W. P. Jones, LES of turbulent flow past a swept fence. Int. J. Heat Fluid Fl. (2003) 24, 606-615.

[22] F. Porte-agel, C. Menevau, M. Parlange, A scale-dependent dynamic model for large-eddy simulation: application to a neutral atmospheric boundary layer. J. Fluid Mech.415 (2000) 261-284.

[23] D. K. Lilly, The representation of small scale turbulence in numerical simulation experiments, *Proceedings of the IBM Scientific Computing Symposium on*

Environmental Sciences, Goldstine H. H. (Ed.), IBM Form **1967**, No. 320-1951, p195-210.

[24] R. Cheesewright, G. McGrath, D. Perry, LDA measurements of turbulent flow in a duct of square cross section at low Reynolds number. Aeronautical Engineering Dept. Rep. ER 1011, Queen Mary Westfield College, Univ. of London, London (1990).

[25] F. B. Gessner, J. K. Po, A. F. Emery, Measurement of developing turbulent flow in a square duct. In Turbulent Shear Flows **I** (1979)119-136. Springer.

[26] F. B. Gessner, A. F. Emery, The numerical prediction of developing turbulent flow in rectangular ducts. J. Fluid. Eng. - T ASME 103(1981) 445-455.

[27] R. A. Antonia, M. Teitel, J. Kim, L. W. Browne, Low-Reynolds-number effects in a fully developed turbulent channel flow. J. Fluid Mech. 236 (1992) 579-605.

[28] J. L. Balint, J. M. Wallace, P. Vukoslavcevic, The velocity and vorticity vector fields of a turbulent boundary layer. Part 2: Statistical properties. J. Fluid Mech. 228(1991) 53-86.

[29] R. D. Moser, J. Kim, N. N. Mansour, Direct numerical simulation of turbulent channel flow up to Rz=590. Phys. Fluids 11(1999) 943-945.

Table 1 Works considered for duct flow

Reference	Investigation	Re_b	Re_τ
Huser & Biringen [16]	duct, DNS	10 320	600
Madabushi & Vanka [10]	duct, LES	5810	360
Gavrilakis [8]	duct, DNS	4410	300
Gessner et al. [25]	duct, experiment	250 000	10550
Brundrett & Bains [12]	duct, experiment	83 000	3860
Cheesewright et al.[24]	duct, experiment	3700	

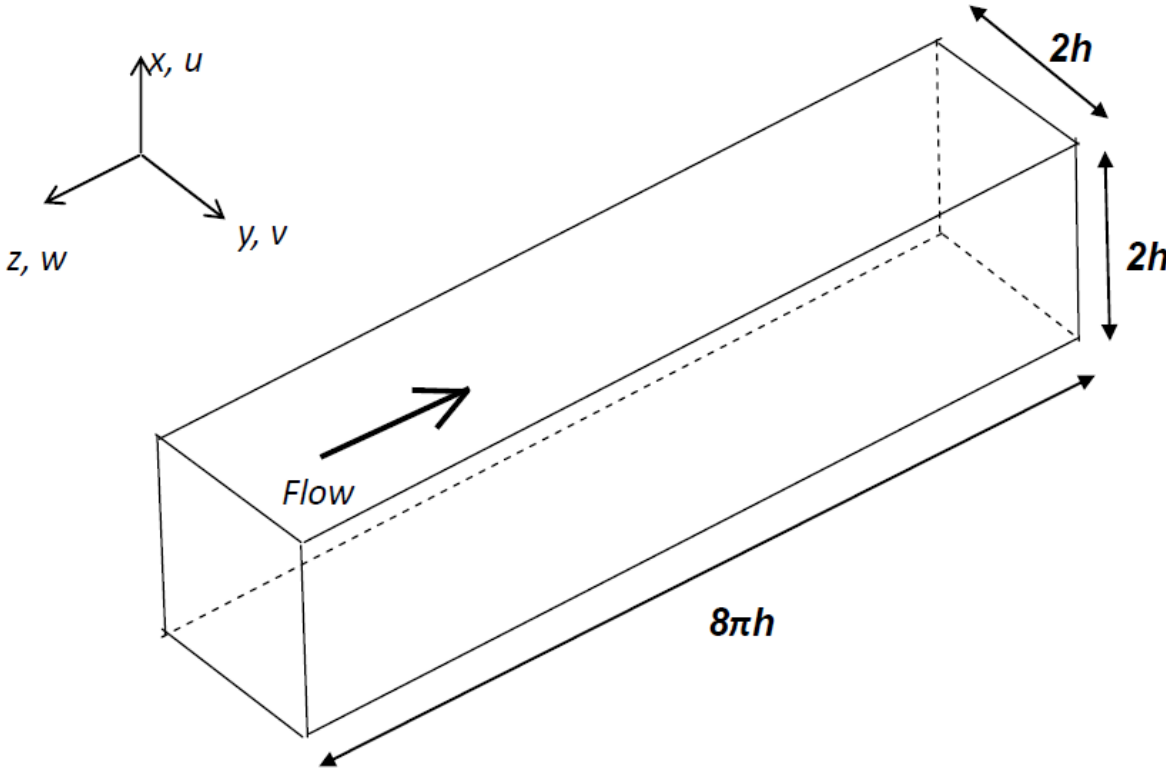

Fig. 1. Schematic of the computational domain.

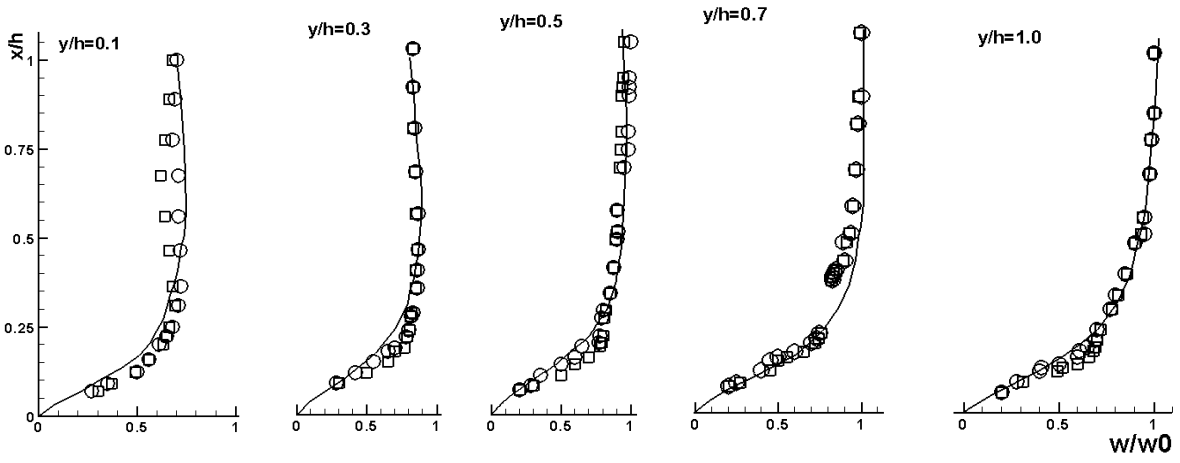

(a)

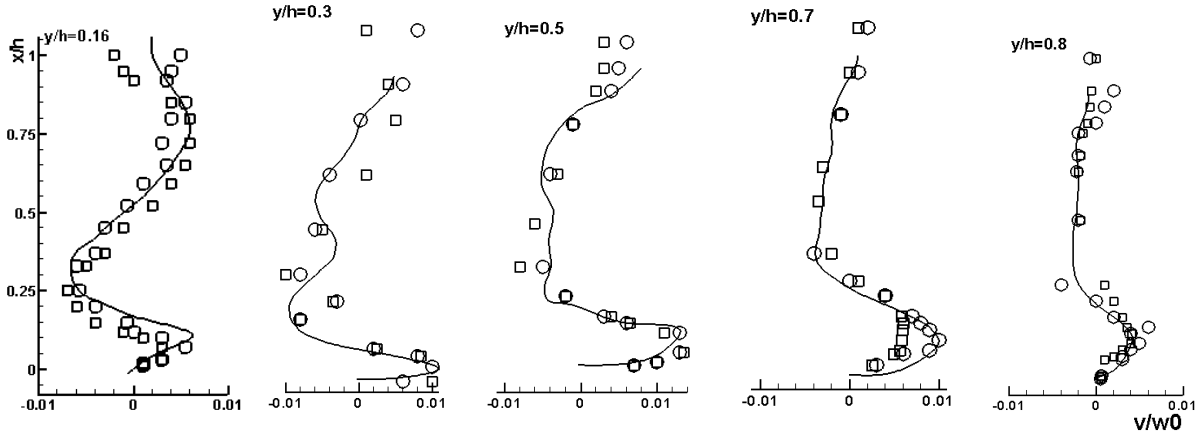

(b)

Fig. 2. Comparison of the simulated mean velocity profiles with the square-duct measurements of Cheesewright et al [24] and DNS of Gavrilakis [8]: (a) streamwise velocity ; (b) spanwise velocity, —, quadrant-averaged simulation data;○, experiment; □, DNS, $Re_b = 4410$.

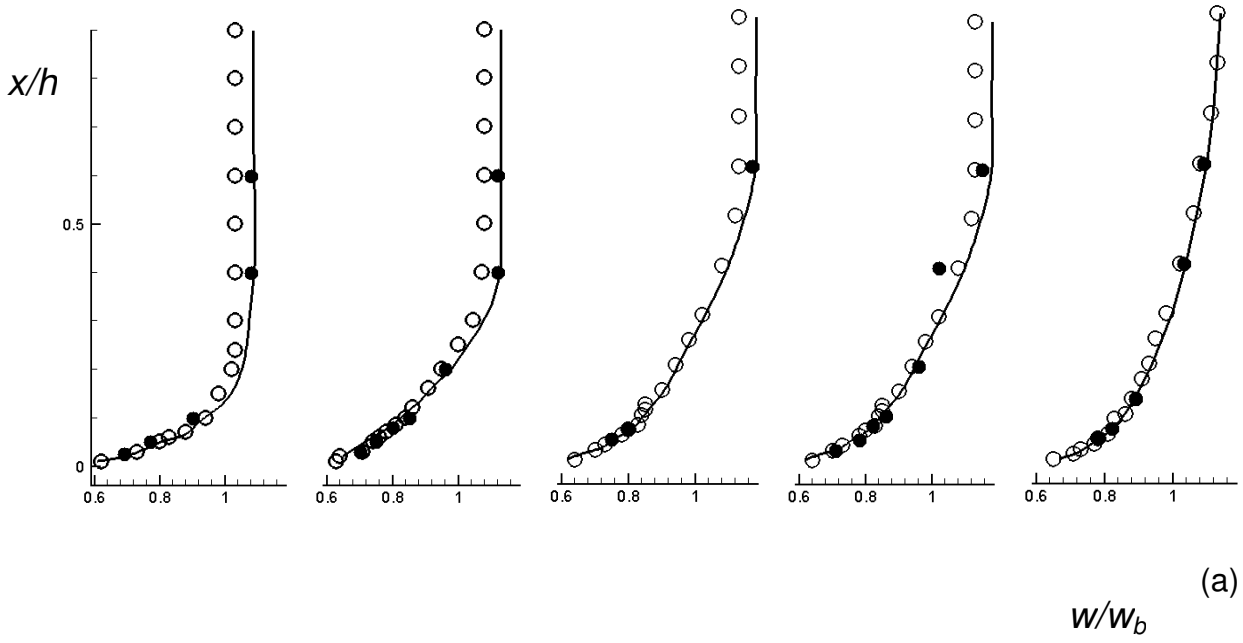

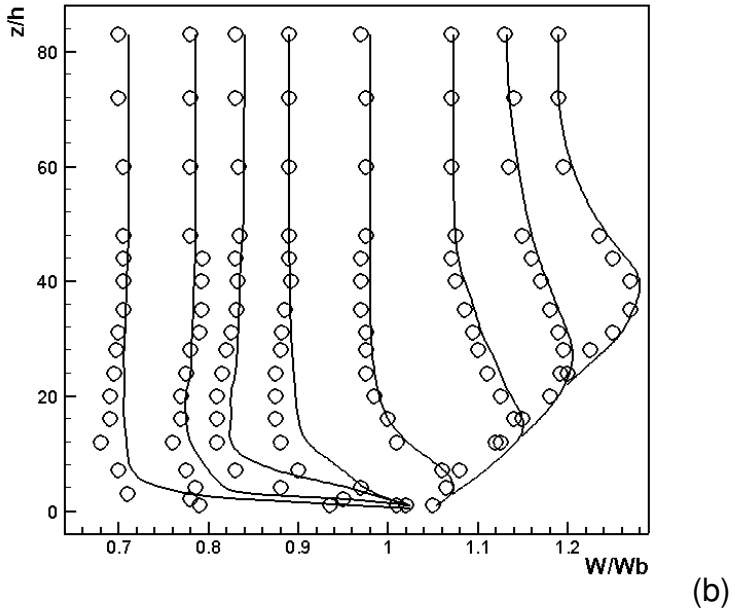

Fig. 3 (a) Streamwise mean velocity distributions along the lower wall bisector for five *z*-planes (from left to right) *z*/h=8,16,24,40 and 84. Values are normalized by the bulk velocity (W_b) for mean steamwise velocity (W). ● Gessner and Emery [26]; ○ Gessner et al. [25]; — present LES results , Re_b=250000. (b) Comparison between the results of the present LES (—) and measurement of Gessner et al. [25] (○) for eight *x*-planes (from left to right) *x*/h=0.01,0.02,0.03,0.05,0.1, 0.2,0.3 and 0.5. Values are normalized by the bulk velocity (W_b) for mean steamwise velocity (W). Re_b=250000

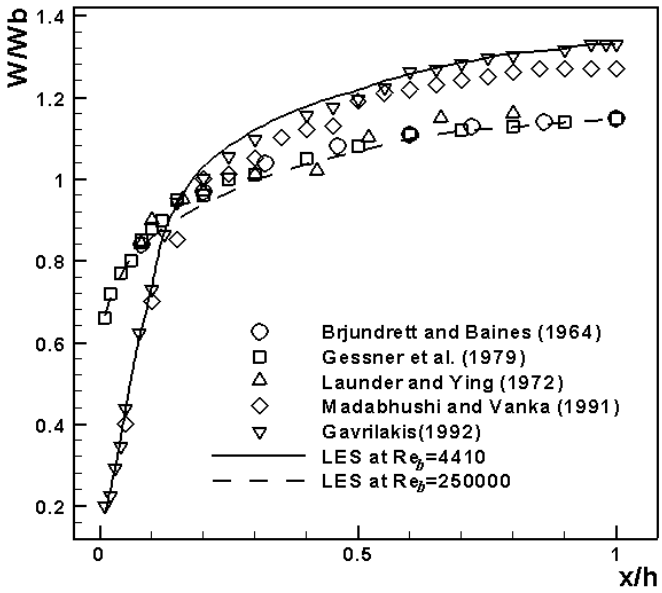

Fig. 4 Streamwise mean velocity distribution along the lower wall bisector at different Reynolds numbers. Brundrett and Baines [12] at Re_b=83000; Gessner et al. [25] at Re_b=250000; Launder and Ying [6] at Re_b =215000; Madabhushi and Vanka [10] at Re_b =5810 and Gavrilakis [8] at Re_b =4410.

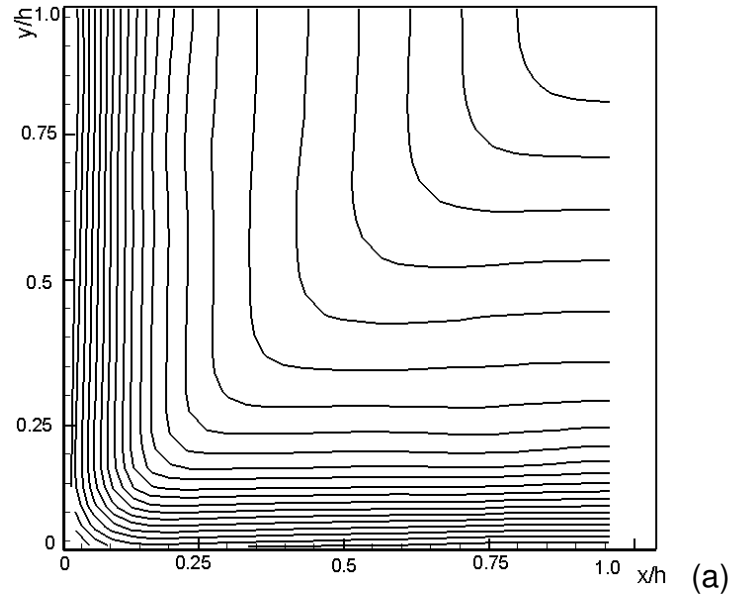

(a)

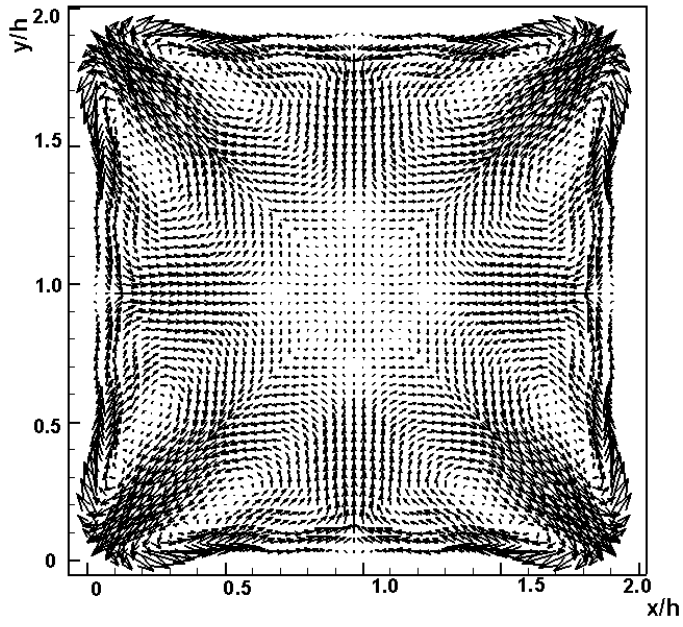

(b)

Fig. 5 Secondary flow at Re_b =35500 (a) contours of mean streamwise velocity; (b) mean secondary velocity vectors in the cross-sectional plane.

.

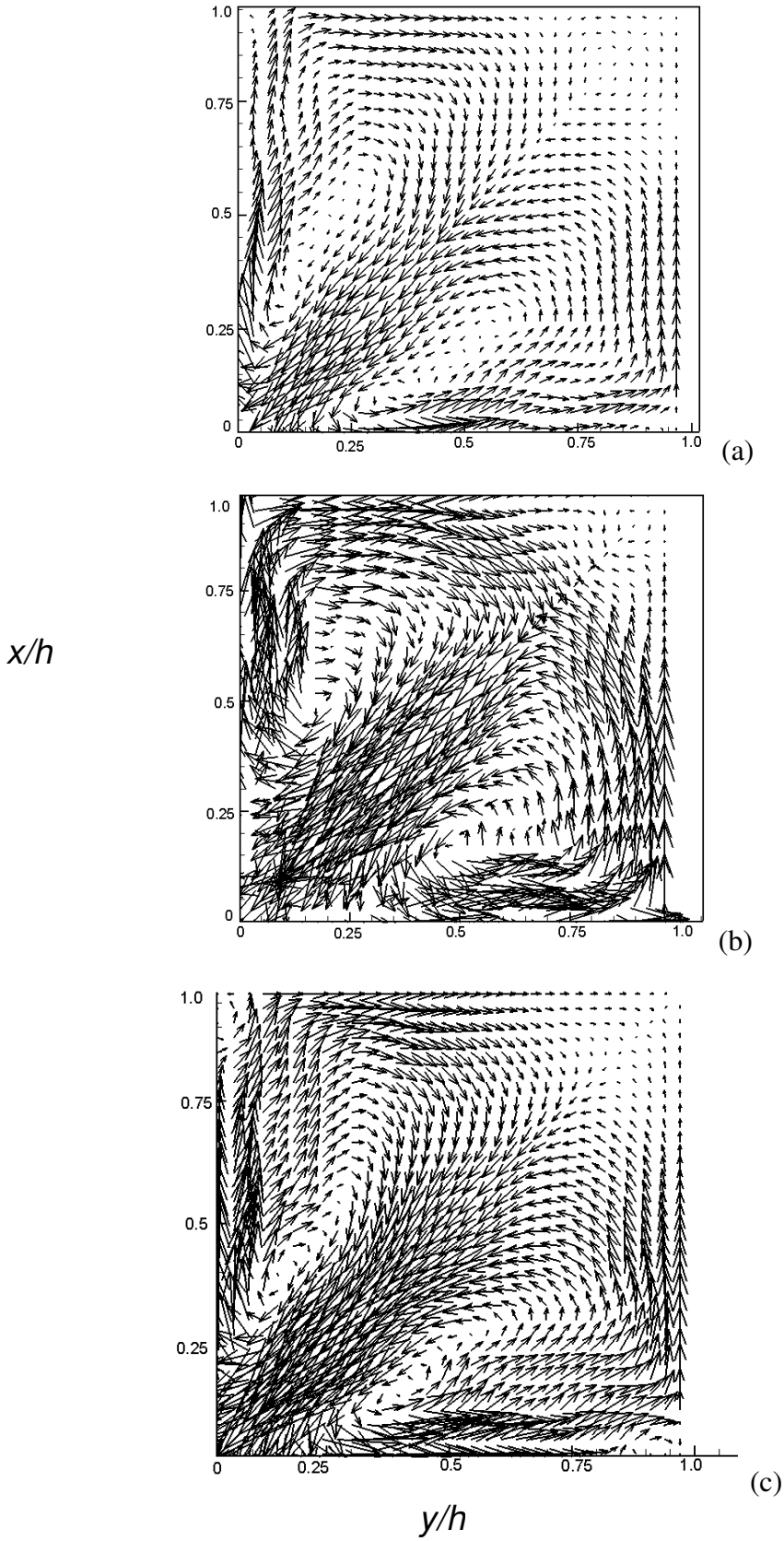

Fig. 6**.** Secondary velocity vectors for Re_b = (a) 10320; (b) 83000; (c) 250000.

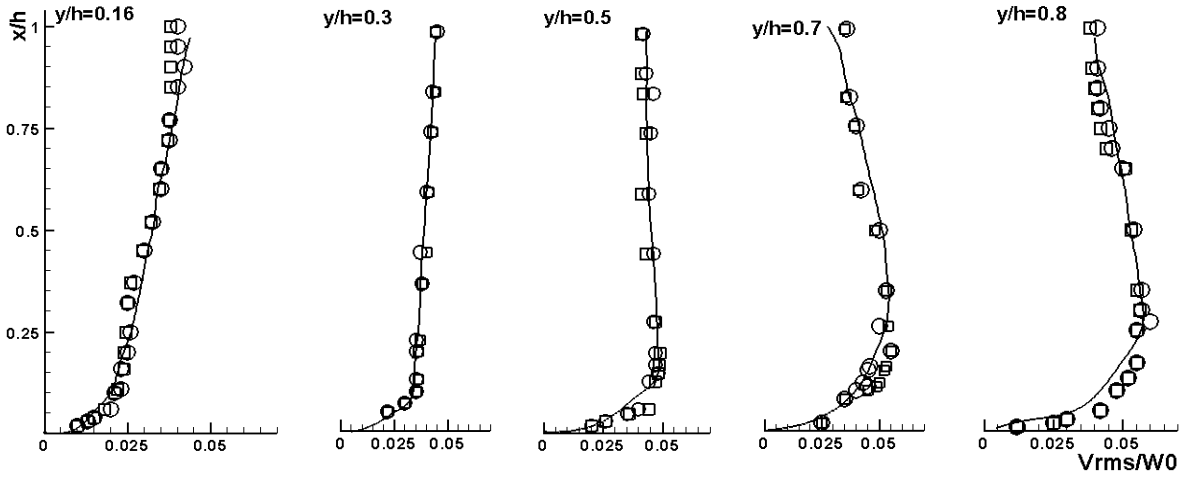

(a)

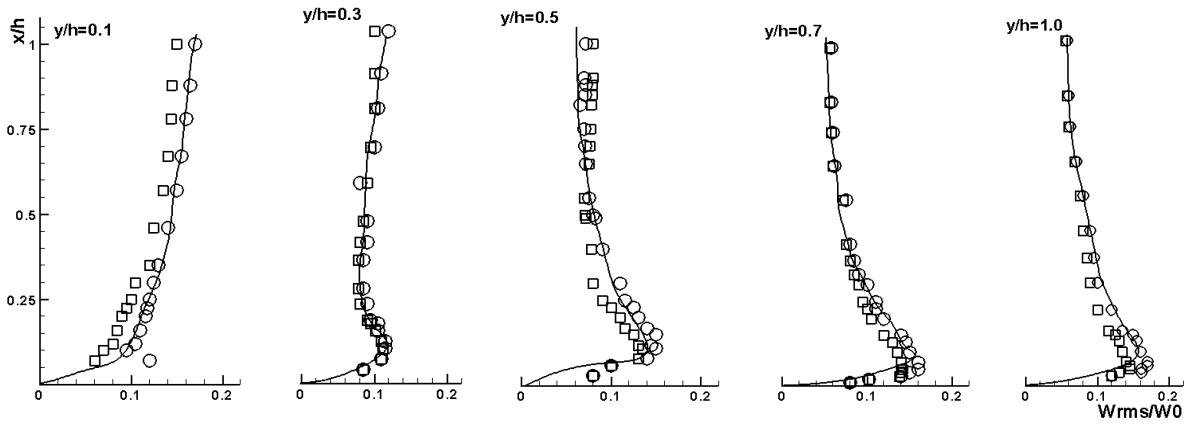

(b)

Fig. 7 Velocity intensities across a duct quadrant: (a) V_{rms}/W_0; (b) W_{rms}/W_0. —, Quadrant average from duct simulation; ○, Cheesewright et al. [24]; □, DNS of Gavrilakis [8], $Re_b = 4410$.

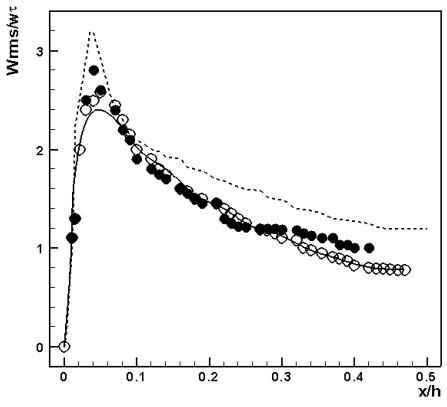

(a)

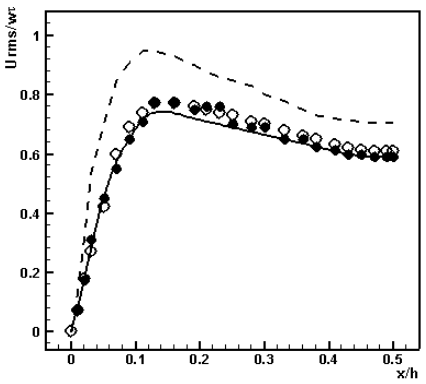

(b)

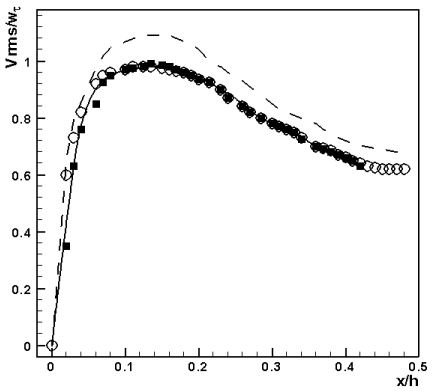

(c)

Fig. 8 Turbulence intensities at the wall bisector: —, present LES at Re_b=4410;----, present LES at Re_b=250000; ○, Gavrilakis[8] DNS at Re_b =4410;●, Cheesewright et al.[24] experiment at Re_b =4410.

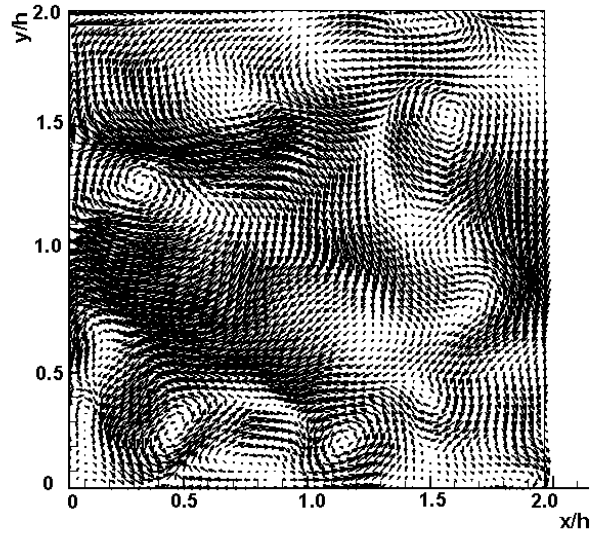

(a)

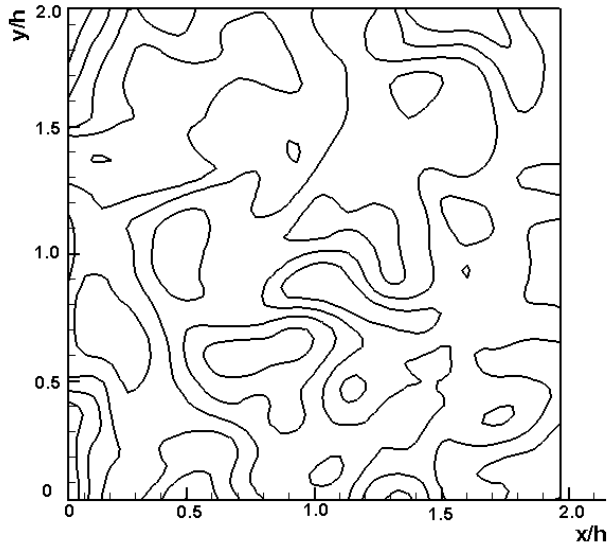

(b)

Fig. 9 Instantaneous secondary velocity and streamwise vorticity distribution in the transverse plane at Re_b=35500: (a) secondary velocity vectors; (b) streamwsie vorticity contous (velocity=0.0016~0.9535, 50 contour levels are given and scaled linearly between the minimum and maximum levels).

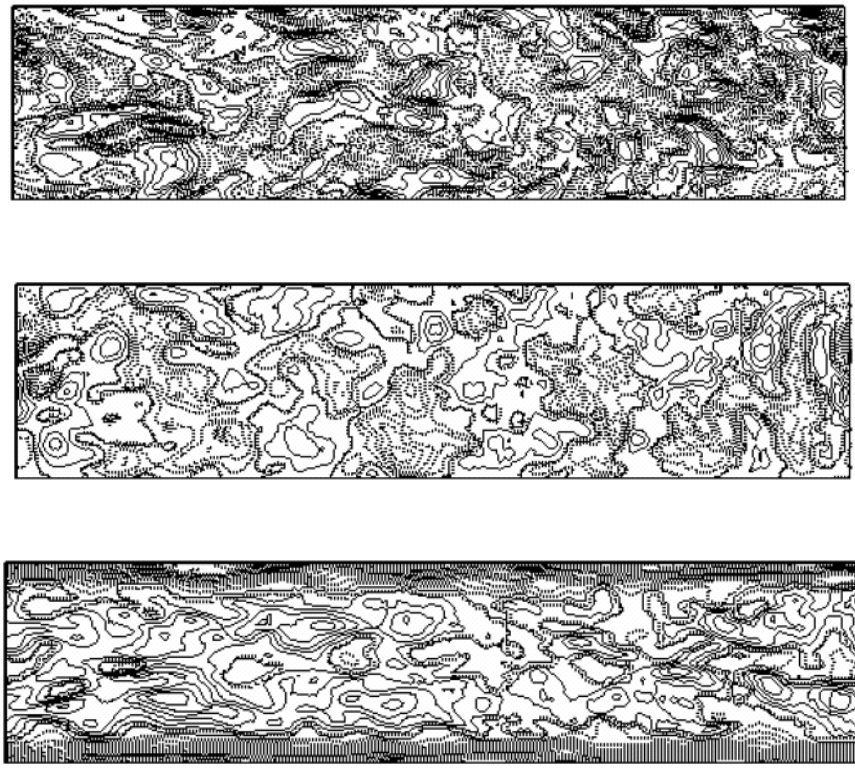

Fig. 10 Instantaneous turbulent fluctuations at x=8,Re_b=35500 : (a) $\overline{u''}$; (b) $\overline{v''}$, and (c) $\overline{w''}$. Legend:—, positive values of velocity; …, negative values of velocity ($\overline{u''}$=-1.27~1.27; $\overline{v''}$=-1.61~1.61; $\overline{w''}$=-2.24 ~2.24, 100 contour levels are given and scaled linearly between the minimum and maximum levels).